Supplement of Clim. Past, 16, 1097–1125, 2020
https://doi.org/10.5194/cp-16-1097-2020-supplement

Climate of the Past
Open Access
EGU

Supplement of

Volcanism and climate change as drivers in Holocene depositional dynamic of Laguna del Maule (Andes of central Chile – 36° S)

Matías Frugone-Álvarez et al.

Correspondence to: Matías Frugone–Álvarez (matutefrugone@gmail.com)

1 Supplementary methods

1.1 Bathymetric survey

Bathymetric surveys were performed based on extensive networks of depth points obtained with a GARMIN GPSmap 178C Sounder. To reconstruct the bathymetric map of the lake, the dataset was resampled, normalized and interpolated in the R environment V. 3.3.0 (R Core Team, 2016), we use the interpolation method known as Universal Kriging (Pebesma, 2004).

1.2 Statistical analysis of XRF data.

Selected elements from XRF Core Scanner (S, Ca, Ti, Mn and Fe) were compared with ICP-MS results and TOC values (Br) to check the correlation of quantitative and semiquantitative (XRF) dataset (Figure S8 and Figure S10). Titanium has been used to “normalize” other elements because of its relatively immobile characteristics after deposition in the lake (Chawchai et al., 2015; Kylander et al., 2011). In order to validate our regression analyses and demonstrate the efficiency of this approach, we used resampling methods (n=100) and calculated the coefficient of determination using the bootstrapping method ($R^2_{boostraping}$) (Kuhn, 2008). We find that the slope of the regression line is significantly different from zero for Fe, Ca, S, Ti, and Mn (Figure S10).

A CONISS analysis routine (Grimm, 1987) was used to define XRF-zones based on the similarity of the data. The results of the CONISS analysis defined eight zones (Figure S8). Two of these coincide with lapilli L2 and L3 and the other with the defined lithostratigraphic units. To investigate the geochemical features of the lake sediments a data set was constructed including only the lacustrine facies values. We tested the assumptions of multivariate normality (Royston’s Multivariate Normality Test) and outlier detection (robust Mahalanobis distances) in the data, but the null hypothesis of multivariate normality was rejected and more of 30 % data are outliers (Figure S7). Thus, the XRF data were

transformed by the natural logarithm function [ln(x)], where x is a XRF raw data or ratio without transformation, so each element was scaled and centered to treat the deviations from the statistical assumptions and apply a multivariate analysis. Consequently, we use a Robust Principal Component Analysis applying the ROBPCA method (Candès *et al.,* 2011; Hubert et al., 2005).

2 Supplementary Results

2.1. Bathymetric survey.

The bathymetric survey identified three main subbasins (Figure 2): 1) a large central subbasin that includes the deepest areas of the lake (up to 60 m), limited to the north by a steep margin, to the east by a series of shallow areas following a N-S trend and including an island, and to the south by a gradual slope towards a large shallow area that occupies the southern third of the lake; 2) a north-western subbasin along a W-E deep trench that follows the topography of the previous fluvial valley; and 3) a northern - eastern subbasin with the deepest areas in the NE bay and progressively shallower towards the south. This bathymetric complexity likely reflects a previous fluvial topography dissecting the previous caldera basin and altered by more recent volcanic activity. Submerged circular-shaped morphologies suggest a previous volcanic landscape flooded by the impoundment of the lake and covered with lacustrine sediments.

2.2. Seismic stratigraphy and sedimentary units

The ca. 20 km of seismic lines acquired with a 3.5 kHz EdgeTech sub-bottom profiler (pinger) were obtained in the central - northern part of LdM Basin, close to main coring sites (Sites 2 and 3) where a denser network was needed. Several longer N-S and E-W profiles were acquired to investigate the main structure of the basin in the deeper areas, and a number of short profiles in the NE bay were designed to check lateral continuity of main reflectors in this area. No seismic images are available to the south of lake (Figure S1 and S2)

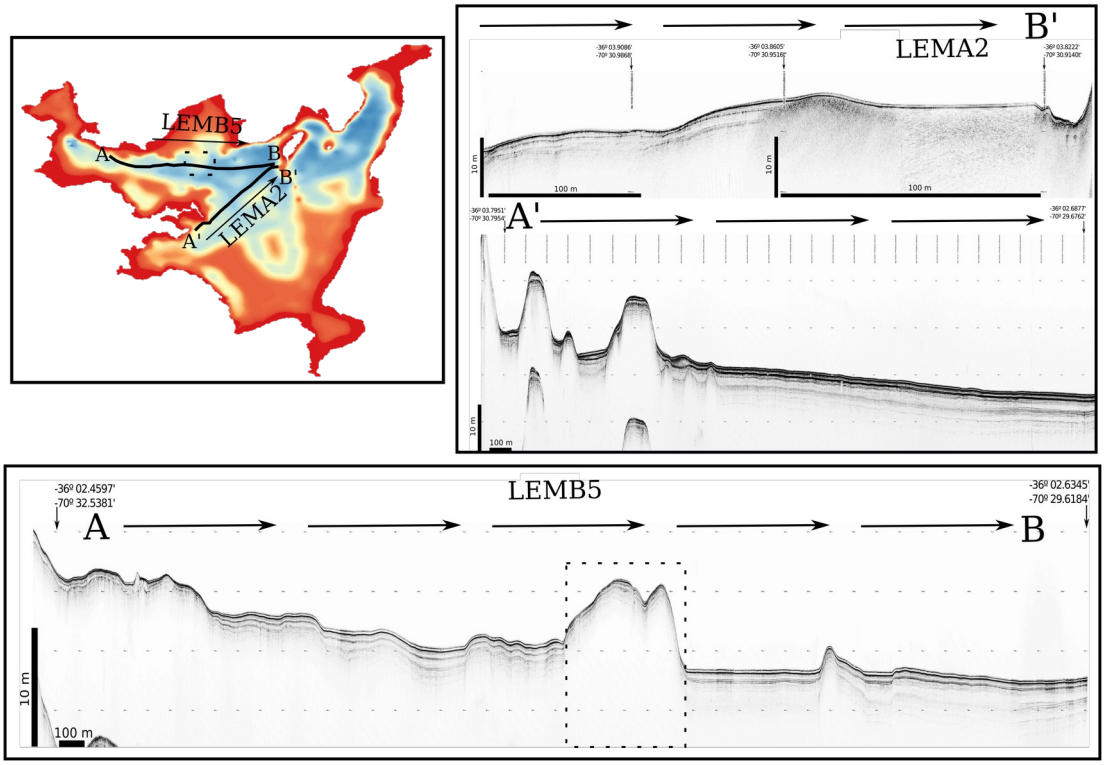

Supplementary Figure S1. LdM map with location of seismic lines NW and Central. Detail of seismic profiles LEMB5 (A to B) and LEMA2 (A'-B').

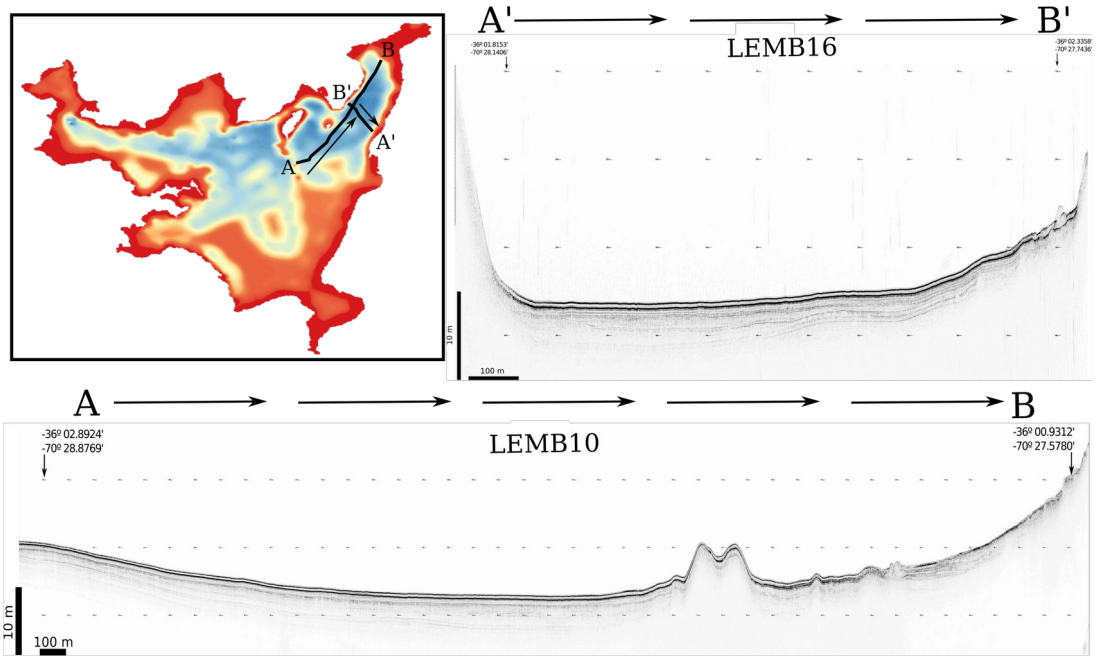

Supplementary Figure S2. LdM map with location of seismic lines NE. Detail of seismic profiles LEMB10 and LEMB16.

Five seismic units have been defined based on the characteristics of seismic reflectors and correlated with lithostratigraphic units. The seismic units correspond to the retrieved sequence including banded to laminated lake sediments with intercalated masswasting deposits (transparent to homogeneous seismic facies) and volcanic layers (main reflectors) and coarse lacustrine/alluvial facies at the base (only reached by coring at site 1)(Figure 6).

Seismic unit S1 is characterized by well defined, parallel reflectors with low-to-high reflection amplitudes, three of them particularly strong that can be followed all over the basin. These high-amplitude bands coincide with T4, the T3-T2 double interval and the uppermost T1 (Figure 6c). The lower limit of the unit is a weaker reflector that could correspond to L2. The unit includes varying seismic facies ranging from low-amplitude to high-amplitude reflections that are all laterally continuous, and more frequent towards the top suggesting more frequent lithological changes. Unit S1 uniformly drapes the whole northern basin, without significant changes in thickness of physical properties even in the northeastern bay (LEMB16). According to the seismic-to-core correlation, S1 encompasses U1 to U3 lithostratigraphic units. Longer seismic profiles (LEMB5, Figure 6) show the lateral continuity of this unit without significant changes in physical properties or thickness in the western part of the basin (closer to Site 1). The southernmost profile (LEMA1) also shows similar structure and thickness for S1. Although top reflectors are equally strong in the eastern part of the basin (LEMB18), S1 seems to thin out towards the East (Figure S2) .

Seismic unit S2 has transparent to low-amplitude seismic facies, and it is more homogeneous in the lowermost section. S2 seems to thin out towards the edges of the basin, both towards the west (LEMB5), the east (LEMB18) and the south (LEMA1). Closer to the Western Peninsula (SW end of LEMA2 profile), S2 maintains a similar thickness and internal structure as in more northern areas. Towards the east (LEMB18), this unit shows thinning and thickening structures, although the low penetration in shallower areas makes it difficult to determine the lower limit of this unit. The presence of this seismically homogeneous unit is not evident in the NE Bay. In the more internal areas of the bay (LEMB15), a relatively more seismically transparent unit below S1 shows a wedge morphology with flat upper boundary, thickening towards the eastern margin and a west- tipping lower boundary with some “channel”- like structure in the western margin indicative of an irregular former topography. In

this NE Bay, normal syn-sedimentary faults in the eastern margin (LEMB16) affect seismic units below S1 (Figure S2). The upper boundary of S2 unit corresponds to a medium-amplitude reflection that correlates with the density contrasts between massive sediments and volcanic facies (T7 and L2). Unit S2 correlates with stratigraphic unit 4 (Lacustrine Turbidite LT1).

Seismic unit S3 is characterized by closely spaced, well-defined although not very strong high-amplitude reflections, wavier than in S1. S3 correlates with stratigraphic unit 5. The stronger reflectors in the upper part of the unit correspond to rapid changes in physical properties in the interval comprising volcanic complex including T9-L3-T8 with intercalated lacustrine sediments (Figure 6c). The relatively strong reflector at the base of the unit corresponds to L5. The thickness of seismic unit S3 is relatively constant in each sub-basin reaching ~ 3 m towards the deepest areas that correspond to the depocenters.

Seismic unit S4 is mostly transparent, with some weak, low amplitude reflections. Only few medium-amplitude reflections occur towards the top of S4, suggesting stronger density contrast. The top of S4 is defined by a weak reflector, with wavy structure that could correspond to the transition from massive (Unit 6) to laminated lacustrine Unit 5. Unit S4 would correspond with the LT2 (Unit 6). The base of unit 6 (seismic unit S4) was only reached in site 1, where it comprises coarse facies (Figure 6c).

Seismic unit S5 shows a relatively strong reflector at the top, mostly continuous and with a wavy pattern (Figure 6b). The reflections below are weakly defined, but they show hummocky and undulated morphologies and lateral discontinuities. Although cores in Sites 2 and 3 did not reach the base of S4, the nature of the basal sediments in Site 1 (coarse sediments ,gravels, fanglomerates, sands with ash and lapilli layers and some fine lacustrine sediments) suggests that the lower sediments of LdM basin are composed of volcanic facies with mass-wasting deposits and coarse littoral/alluvial and lacustrine sediments.

Unit 6 (500-440 cm) is composed of massive black silt facies corresponding to lacustrine turbidite LT2. This unit has been recovered in site 3 (long cores LEM13-3A, LEM13-3E and LEM13-3B), 2 (long core LEM13-2C) and 1 (long core LEM13-1B). In site 2 the core did not reach the base of this unit, so their total thickness and internal structure is unknown (Figure 3).

However, the base of the unit (500-480 cm) has lower TOC, TOC/TN and BioSi values and higher TIC than the upper part (480-440 cm) (Figure 4). Although core recovery was low in the basal drives of Site 1 and sedimentary facies are quite different, the thickness of unit 6 in western site LEM13-1B seems much reduced (5 cm) compared to the eastern site 3. In Site 1 this unit is composed of a coarse basal layer with irregular basal boundary and flat and sharp upper boundary and a top finer layer with similar black silt facies as in Site 3. Coarse basal sediments include gravel-size clasts and a sandy and silty matrix with some reworked fine lacustrine sediments. These mixed and chaotic textures could be an artifact caused by coring. However, the presence of coarse sediments at the base of unit 6 suggests a more proximal location for the emplacement of mass wasting deposit in site 3.

- Sedimentary units.

Unit 6 (500-440 cm) is composed of massive black silt facies corresponding to lacustrine turbidite LT2. This unit has been recovered in site 3 (long cores LEM13-3A, LEM13-3E and LEM13-3B), 2 (long core LEM13-2C) and 1 (long core LEM13-1B). In site 2 the core did not reach the base of this unit, so their total thickness and internal structure is unknown (Figure 3, in the main text). However, the base of the unit (500-480 cm) has lower TOC, TOC/TN and BioSi values and higher TIC than the upper part (480-440 cm) (Figure 4, in the main text). Although core recovery was low in the basal drives of Site 1 and sedimentary facies are quite different, unit 6 thickness in western site LEM13-1B seems much reduced (5 cm) compared to eastern site 3. In Site 1 this unit is composed of a coarse basal layer with irregular basal boundary and flat and sharp upper boundary and a top finer layer with similar black silt facies as in Site 3. Coarse basal sediments include gravel-size clasts and a sandy and silty matrix with some reworked fine lacustrine sediments. These mixed and chaotic textures could be an artifact caused by coring. However, the presence of coarse sediments at the base of unit 6 suggests a more proximal location for the emplacement of mass wasting deposit in site 3.

Unit 5 (440-300 cm) groups laminated facies D6. The lower boundary is sharp and the unit starts with deposition of finely laminated greenish grey facies (D6a) with some

laminae composed almost exclusively by diatoms. This interval shows some variability along the cores, with convoluted grading to parallel lamination and some internal erosive surfaces in core LEM13-3A to parallel lamination in core LEM13-3E and LEM13-3B. The occurrence of T18 allows a correlation between both cores (Figure 3, in the main text). Towards the top of the unit, carbonate-bearing laminated subfacies D6b and dark brown, coarser, macrophyte-rich subfacies D7c alternate. The top of unit 5 is located at the base of the complex volcanic event starting with deposition of T9.

Unit 4 (300-195 cm) is characterized by banded and massive silt facies corresponding to Lacustrine Turbidite LT1. The base of the unit is banded and darker, and with lower TOC content than the upper, massive and homogeneous interval. Occurrence of a thin interval of similar facies within the volcanic event T9–L3–T8 suggests that turbidite processes were multi-phased, with a small event after deposition of the L3 and the larger event after deposition of T8 (Figures 3 and 4). The LT1 unit is capped by an ash layer (T7). This unit occurs in all sites (1, 2 and 3) and maintains similar thickness (ca. 70-80 cm). Core LEM13-2C did not reach the base of this unit, so the thickness is unknown (Fig. 3). In the western site 1B, LT1 thickness is smaller (40 cm).

Unit 3 (195-43 cm) is composed of banded to laminated facies (D3, D4 and D5) grouped in (D3/D5 - D4) and (D5-D3-D4) sequences (Figs. 3 and 4, in the main text). The lower subunit shows a dominance of facies D4 and D5 and the upper unit D3 and D5. The lower limit is the top of T7 and the upper limit is located at the base of T4.

Unit 2 (43–14 cm) is characterized by facies D3 with an intercalation of finer and less organic facies D4. The unit starts after deposition of the conspicu-ous cm-thick double-colored tephra T4-T3 and ends prior to deposition of T1. Up to 8 volcanic-rich layers (facies CT) occur. A short core transect in the northern part of the LdM basin illustrates facies variability in unit 2. Cryptotephras are more frequent and better defined in the western site (core LEM11-1A) and harder to identify in the central (LEM13-3D and LEM13-3C) and eastern

(LEM13-3A and 3B) areas. Banded facies D3 are more macrophyte-rich in the shallower core LEM11-3A (24 m water depth) compared to deeper areas.

Unit 1 (0-14 cm) is made of finer, less organic facies D1 and D2 compared to underlying unit 2. The base of the unit is T1. The core transect shows similar facies and sediment composition trend (facies D1 at the base and facies D2 towards the top) in the northern part of the basin, from shallower to deeper sites, and also in the southern areas (LEM12-4A). A small increase in TOC at the very top of the sequence is detected in some cores from the western (LEM11-1A), eastern (LEM13-3D) and southern (LEM12-4A) sites. A cryptotephra layer (facies CT) is also found in cores in the northern sites at the top of the sequence.

General stratigraphy of Site 1 for the upper 5 units is similar to Site 3 (Figures 3), suggesting that the composite stratigraphy of site 3 is representative of the sedimentary infill in the northern areas of the basin. Core LEM13-1B (31 m water depth) reached 5.8 m below lake floor, recovering 2.5 m of lacustrine sediments and volcanic facies below laminated unit 5. Unit 6 (LT2) in this shallower, western site is composed of: i) a thick (60 cm) basal layer composed of gravel and sands with abundant silty matrix with erosive and irregular lower boundary and flat, abrupt upper boundary. Absence of grading and sorting, presence of grain sizes from sand to fine silt and abundance of matrix suggest an emplacement as high density flow (fanglomerates?). However, as pointed out previously, recovery of this interval is poor, so textural and sedimentological diagnostic features could not be identified; ii) a thin (14 cm) homogeneous and massive top layer, with similar massive facies that characterize LT2 in site 3.

Sediments below Unit 6 in site 1 have been grouped in stratigraphic unit 7. It includes coarse clastic facies, fine lacustrine laminated sediments, a thin lapiili (L6, 25 cm) and five tephras (T19 to T23). The base of the core is composed by a coarse breccia (110 cm) with angular cm-long volcanic clasts in a volcanic matrix. It likely represents brecciated volcanic facies (lava flows?) emplaced in the distal areas of the lake. Laminated diatomaceous facies

(25 cm) cover this basal breccia with an intercalated thick, black, mafic-rich tephra (T23). Although recovery of the sediment is low and some coring artifacts (sediment mixing, irregular boundaries) occur, the presence of a thick interval (35 cm) of homogeneous coarse sands with clay/silt matrix at the base and coarse gravels with unsorted sandy matrix at the top suggest that coarse materials were intercalated with fine lacustrine facies and ash fall deposits. The rounded nature of the clasts argue for a fluvial/alluvial transport previous to deposition in the profundal areas of the lake. The upper part of Unit 7 includes laminated diatomaceous facies with several thin tephras (T21 to T19) and one Lapilli (L6).

3. Supplementary Table

Supplementary Table S1. Location (latitude and longitude), length and depth for the LdM cores.

ID cores	Latitude(UTM)	Longitude(UTM)	Length(m)	Depth(m)	Coring system
CHILL-LEM13-1A	6010754	360391	1.82	31	Uwitec-Piston Corer
CHILL-LEM13-1B	6010732	360401	6.07	31.5	Uwitec-Piston Corer
CHILL-LEM13-3B	6010066	365499	4.60	46.5	Uwitec-Piston Corer
CHILL-LEM13-3E	6010153	365464	5.02	46.5	Uwitec-Piston Corer
CHILL-LEM13-2C	6009829	364405	3.41	44.5	Uwitec-Piston Corer
CHILL-LEM13-3A	6010196	366548	4.70	46.5	Uwitec-Piston Corer
CHILL-LEM13-1C-1G	6010760	360302	0.49	31	Gravity Corer
CHILL-LEM13-1D-1G	6010760	360302	0.50	31	Gravity Corer
CHILL-LEM13-2A-1G	6009829	364405	0.52	44	Gravity Corer
CHILL-LEM13-2B-1G	6009829	364405	0.52	44	Gravity Corer
CHILL-LEM13-3C-1G	6010066	365499	0.52	44	Gravity Corer
CHILL-LEM13-3D-1G	6010066	365499	0.49	44	Gravity Corer
CHILL-LEM13-4A-1G	6010437	364084	0.46	38	Gravity Corer
CHILL-LEM13-5A-1G	6010452	362544	0.58	8.5	Gravity Corer
CHILL-LEM13-6A-1G	6010580	361595	0.54	7.5	Gravity Corer
LEMAL-LEM11-1A-1G	6010779	360347	0.48	46	Gravity Corer
LEMAL-LEM11-2A-1G	6011009	359828	0.22	58	Gravity Corer
LEMAL-LEM11-3A-1G	6010520	360903	0.79	24	Gravity Corer
MAUEN-LEM12-1A-1G	6013809	368543	0.30	43	Gravity Corer
MAUEN-LEM12-2A-1G	6009359	364314	0.43	43	Gravity Corer
MAUEN-LEM12-3A-1G	6010934	366586	0.21	48	Gravity Corer
MAUEN-LEM12-3B-1G	6010934	366586	0.29	48	Gravity Corer
MAUEN-LEM12-4A-1G	6006964	366212	0.25	31	Gravity Corer

Supplementary Table S2. Robust Principal component analysis of the XRF core scanner dataset. Loadings by factor, eigenvalue and importance of each component.

Factor	**PC1**	**PC2**	**PC3**
Si	0.2608	0.0210	0.4590
S	0.0991	0.2099	0.2979
K	0.3102	-0.1442	0.3759
Ca	0.3557	0.1632	0.2817
Ti	0.3326	-0.4067	0.1840
Mn	0.1131	0.6255	0.0541
Fe	-0.2327	-0.2228	0.4240
As	-0.3026	0.0987	0.3576
Br	0.1118	0.4988	0.0394
Rb	0.3970	-0.0432	-0.1872
Sr	0.3245	0.1028	-0.2481
Zr	0.3935	-0.1756	-0.1932
Eigenvalues	5.12	1.99	1.60
Standard deviation	2.26	1.41	1.26
Proportion of Variance	0.59	0.22	0.18
Cumulative Proportion	0.58	0.81	1.00

Supplementary Table S3. ^{210}Pb and ^{137}Cs activities, date established using constant rate of supply (C.R.S) model from core LEM12-3B and number of *Pinus radiata* pollen.

Depth(cm)	^{137}Cs (pC_i/g)	Total ^{210}Pb Activity (pC_i/g)	^{210}Pb Cum. Act. Below Int.(pC_i/cm^2)	Date (A.D.)	Error of age (yr)	Nº Pinus Pollen
0.5	--	4,5359	6,1918	2011.1	2.3	--
2.5	--	3,0670	4,7346	2002.5	2.2	--
4.5	0.12	4,1777	2,9221	1987.0	2.6	3
5.5	0.18	3,5391	2,0721	1976.0	3.3	16
6.5*	0.40	2,5582	1,4693	1964.9	4.0	--
7.5	0.34	1,686	1,091	1955.4	4.9	--
8.5	0.25	1,2508	0,8589	1947.7	6.0	45
10	--	0,9481	0,5976	1936.1	7.9	24
11	--	0,9707	0,428	1925.3	10.8	--
12	--	1,0573	0,2232	1904.4	20.35	--
13**	--	1,21	–	--	--	--
13.5***	--	0,5474	--	--	--	0
14***	--	0,4387	--	--	--	0
15	--	0,36	--	--	--	0
16.5	--	0,7706	--	--	--	13
18	--	0,8317	--	--	--	0
23	--	0,7711	--	--	--	0
30		0,7746	--	--	--	0

* ^{137}Cs Peak (1963)

** Supported 210Pb: 0.5397 ± 0.0734 pCi/g

*** Quizapú ash layer (CE 1932)

--: no data

Supplementary Table S4.

Ran on Sat May 2 09:48:51 2015

Calibration curves (cc) 3 : SHCal13;

id	yr	std	depth	d.R	d.STD	t.a	t.b	cc
Pb-210	-61.1	2.32	0	0	0	3	4	0
Pb-210	-52.5	2.23	2	0	0	3	4	0
Pb-210	-37	2.64	4	0	0	3	4	0
Pb-210	-26	3.27	5	0	0	3	4	0
Pb-210	-14.9	4.07	6	0	0	3	4	0
Pb-210	-5.4	4.96	7	0	0	3	4	0
Pb-210	2.3	6.04	8	0	0	3	4	0
Pb-210	13.9	7.94	9.5	0	0	3	4	0
Pb-210	24.7	10.86	10.5	0	0	3	4	0
Pb-210	45.6	20.35	11.5	0	0	3	4	0
T1	19.5	5	12	0	0	3	4	0
Poz-57545	85	25	13	0	0	3	4	3
Poz-59915	4820	60	14	4700	60	3	4	3
133687	680	35	38	0	0	3	4	3
Poz-59917	8230	50	157	4700	60	3	4	3
Poz-59918	8500	50	158	4700	60	3	4	3
Poz-59919	11440	60	200	4700	60	3	4	3
Poz-59921	12550	70	213	4700	60	3	4	3
Poz-59922	14000	70	234	4700	60	3	4	3
Poz-59923	15630	130	259	4700	60	3	4	3

R code

```
source('Bacon.R')
Bacon("LEM", acc.mean=80, res=20, acc.shape=1.5, mem.strength=4, mem.mean=0.7, thick=4,d.by=0.4, ssize=8000, d.max=268, rotate.axes=TRUE)
dev.off()
```

4. Supplementary Figures.

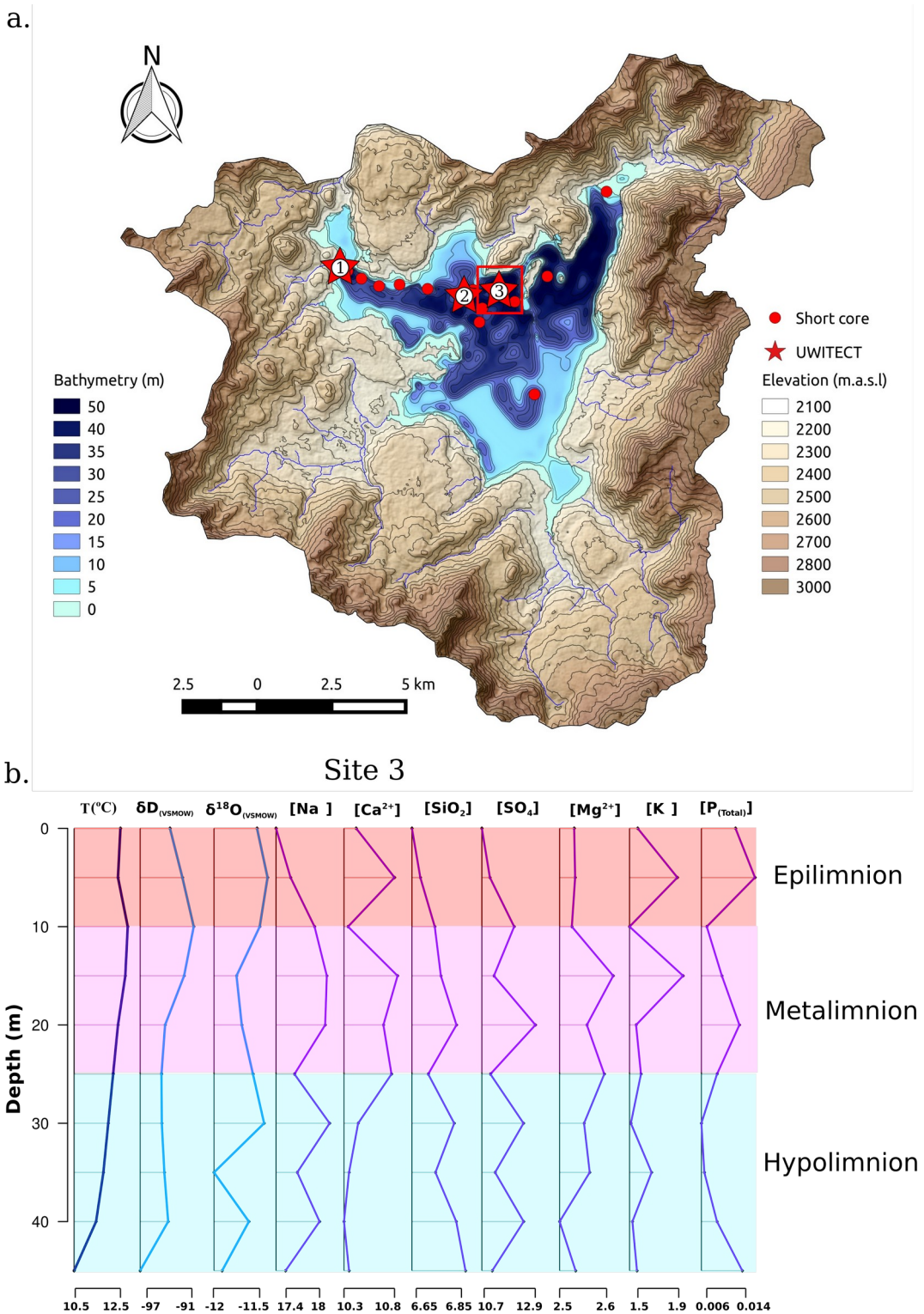

Supplementary Figure S3. Hydrology LdM. a) Catchment basin and drainage area of LdM. b) Depth profile (March 2013) of temperature, isotopic and main cation and anion chemical composition of LdM.

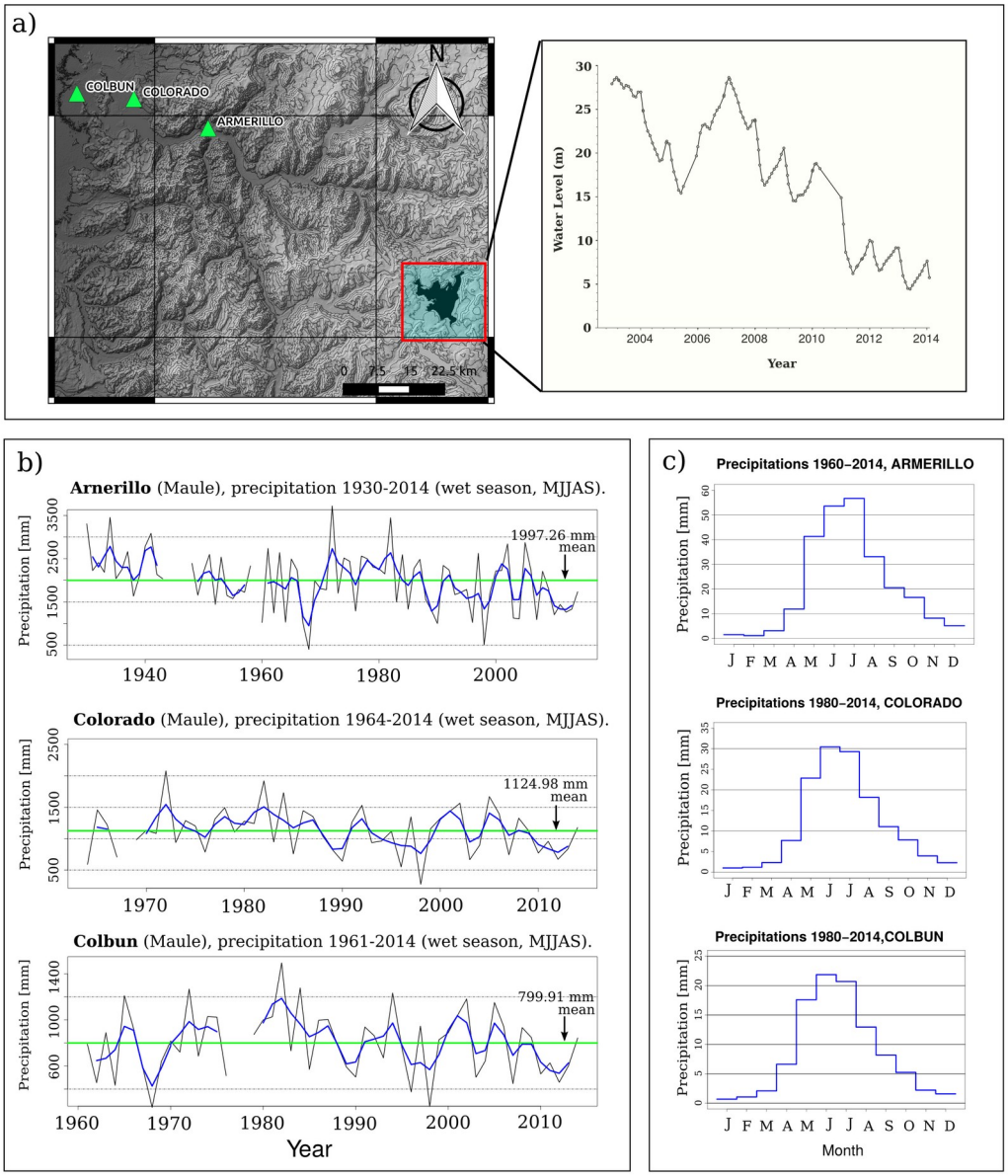

Supplementary Figure S4. Meteorological data from LdM. a) Location map of LdM, nearby weather station and LdM water levels fluctuate between 2002 and 2014; Mean lake level with respect to the dam during the last decade. b) monthly average precipitation for the months of May, June, July, August and September for Colbun (280 m asl.), Colorado (420 m asl.) and Armerillo (520 m asl.). c) Climograph of precipitation for Colbun, Colorado and Armerillo. Note the increase in rainfall with elevation.

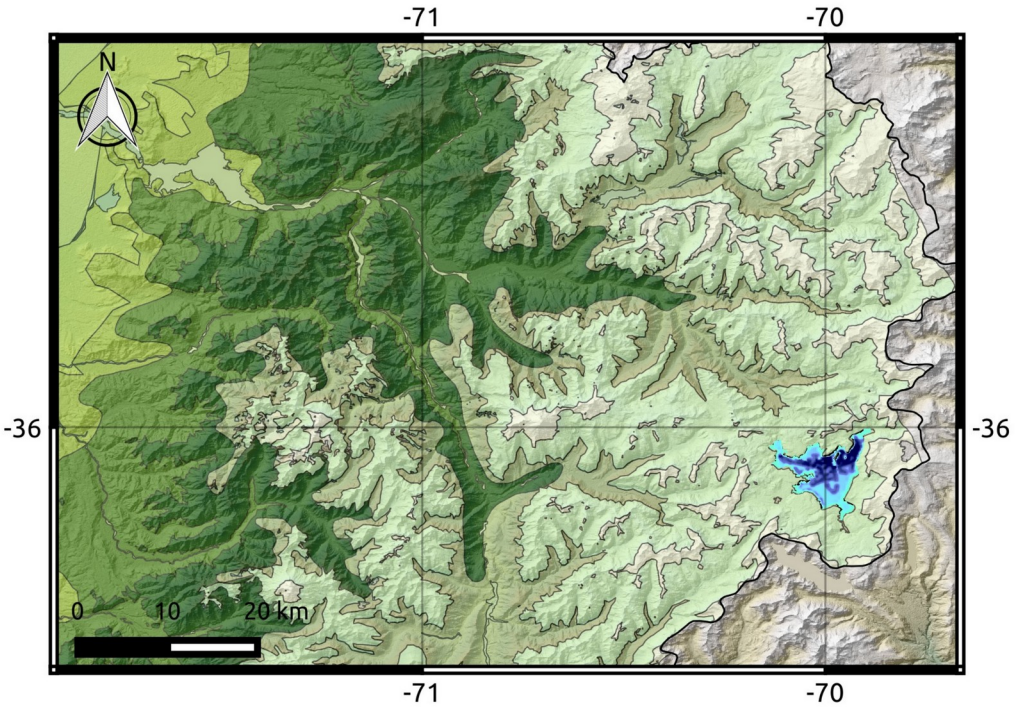

Vegetation Belts

- Deciduous Mediterranean Andean forest dominated by *Nothofagus oblinqua* and *A. chilensis*
- Deciduous Mediterranean Andean forest dominated by *Nothofagus glauca* and Nothofagus obliqua
- Esclerofilous Mediterranean Andean forest dominated by *Lithrea caustica* and *Lomatia hirsuta*
- Esclerofilous Mediterranean Andean forest dominated by *Lithrea caustica* and *Peumus bolbus*
- Mediterranean Andean shrubland dominated by *Oxalis andenophylla* a nd *Pozoa coriacea*
- Mediterranean Andean shrublands dominated by *Chuquiraga oppositifolia* and *Discaria articulat*a
- Mediterranean Andean shrublands dominated by *Laretia acaulis* and *Berberis empetrifolia*

Supplementary Figure S5. Vegetation Map of LdM region (adapted from Luebert and Pliscoff, 2006)

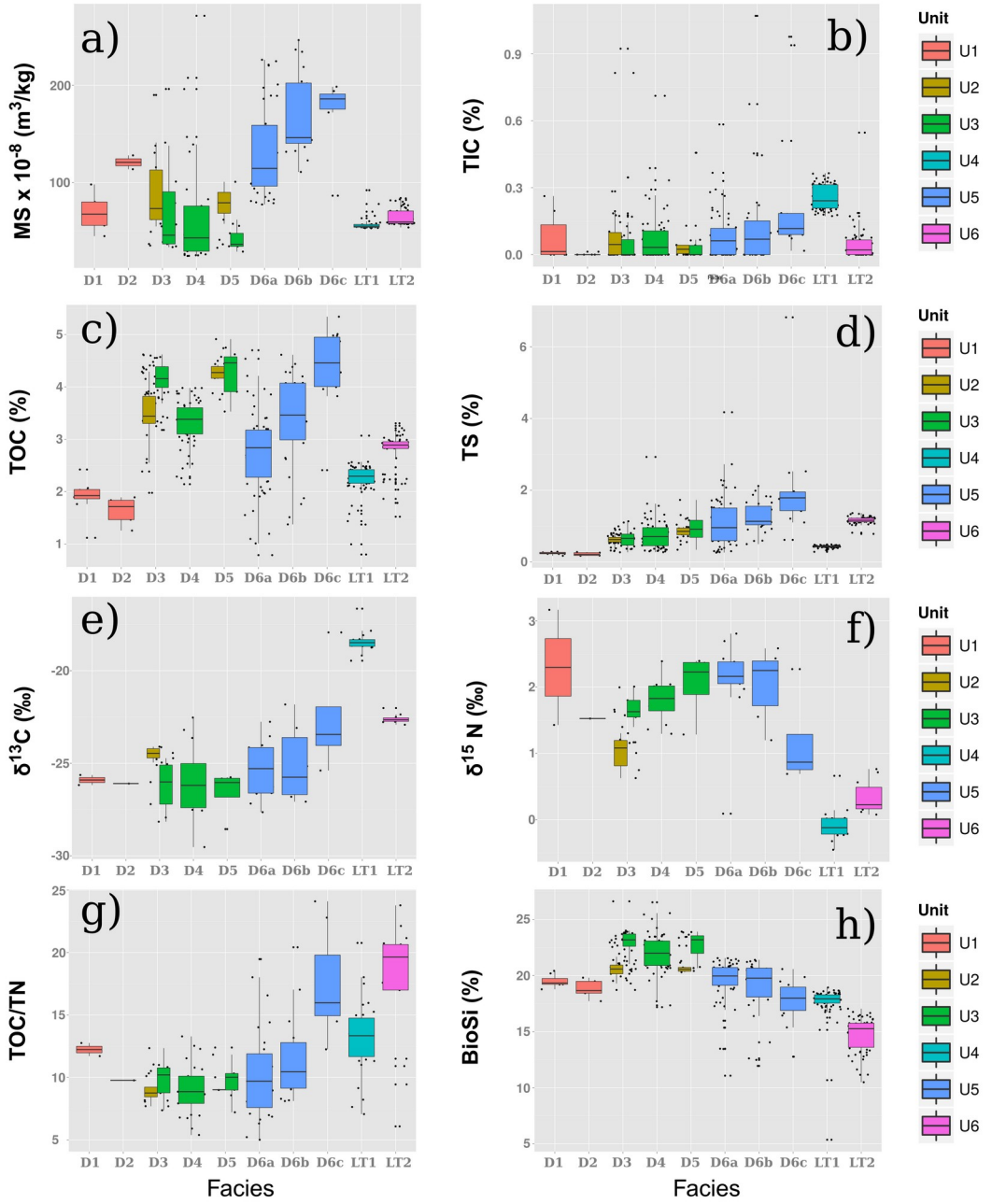

Supplementary Figure S6. Boxplots of sedimentary facies composition. a) Magnetic Susceptibility; b) Total Inorganic Carbon; c) Total Organic Carbon (%); d) Total Sulphur ; e) $\delta^{13}C$ f) $\delta^{15}N$; g) TOC/TN atm; h) BioSi. The data were plotted with the R *qqplot* package (Wickham, H., and Chang, W. 2013)

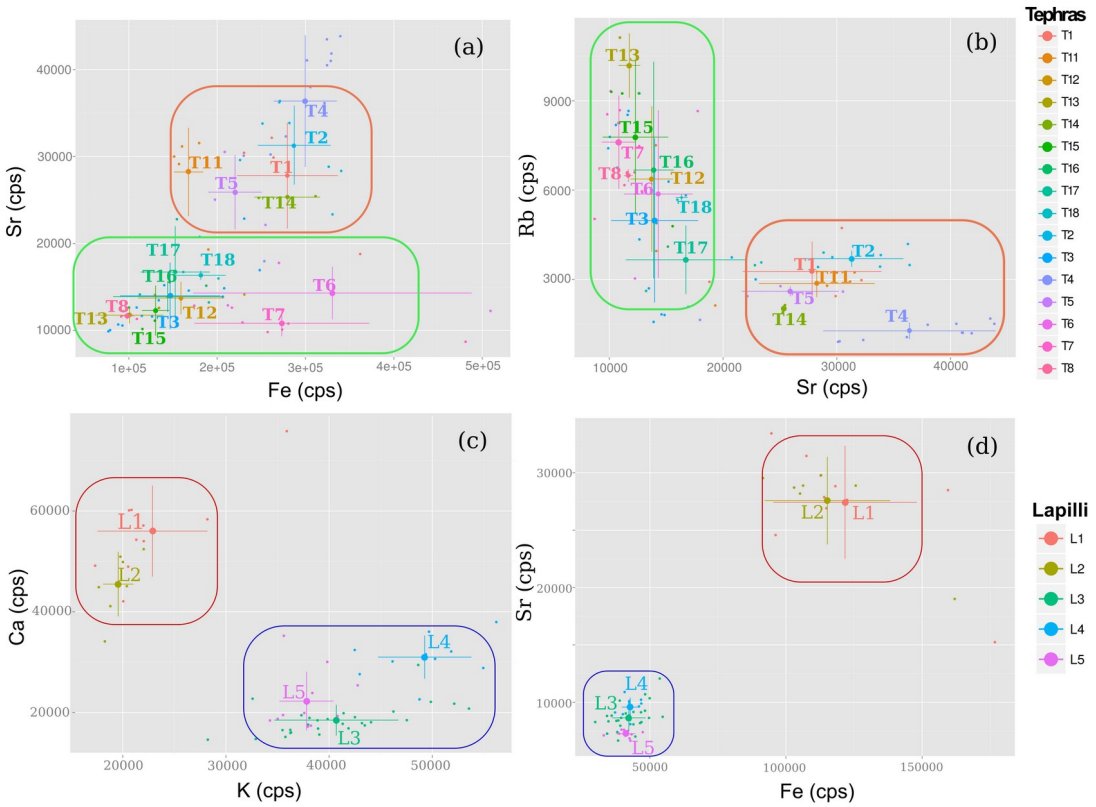

Supplementary Figure S7. a) Sr (cps) vs Fe (cps) values for Tephras (T1 to T18); b) Rb (cps) vs Sr(cps) values for Tephras (T1 to T18); c) Ca (cps) vs K (cps) values for Lapillis (L1 to L5); Sr (cps) vs Fe (cps) values for Lapillis (L1 to L5). Large dots and line indicate the mean and standard deviations, respectively. The data were plotted with the R *qqplot* package (Wickham, H., and Chang, W. 2013)

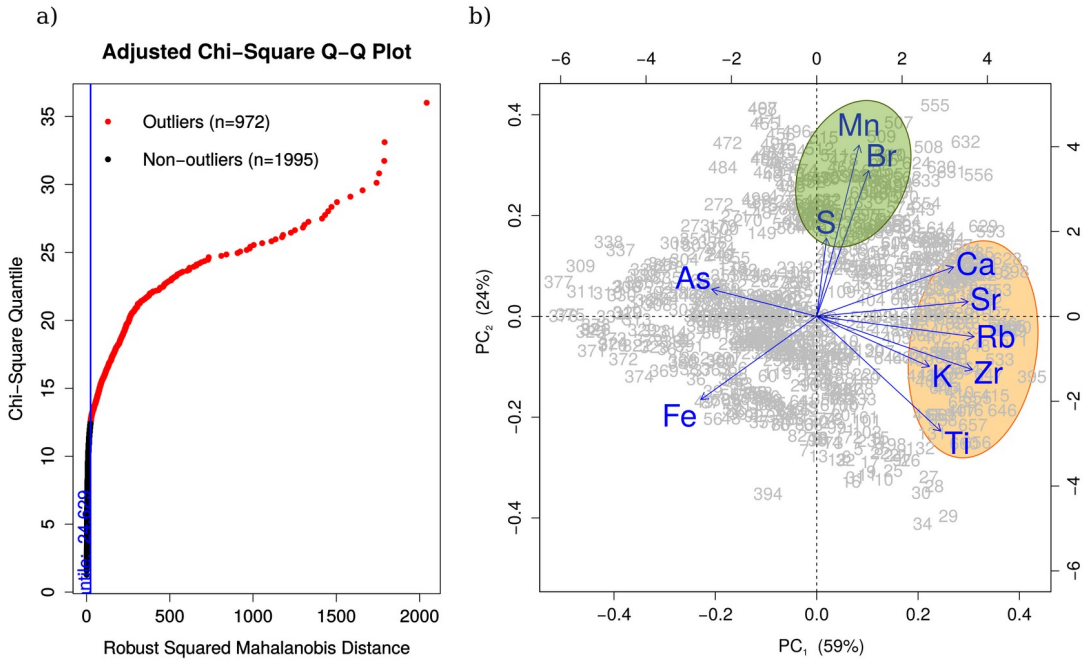

Supplementary Figure S8. Biplot associated to the Robust Principal Component Analysis (RPCA) of XRF data (> 1000 cps)from LdM. We tested the assumptions of multivariate normality (Royston's Multivariate Normality Test) and outlier detection (robust Mahalanobis distances) in the data, the null hypothesis of multivariate normality was rejected and more of 30 % data are outliers. The first eigenvector is interpreted as sediment delivery and the second eigenvector as a productivity index. RPCA use the ROBPCA method (Hubert et al., 2005).

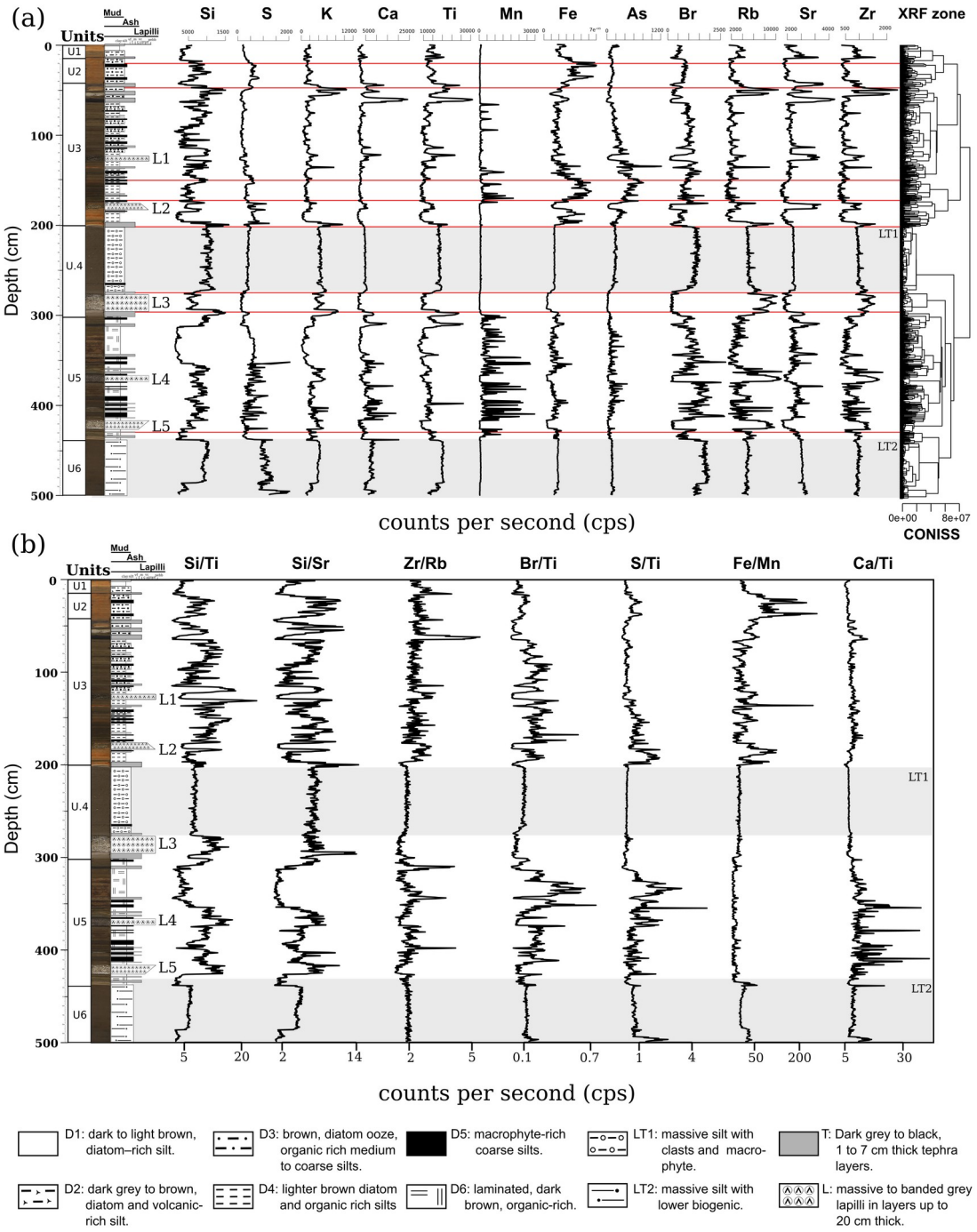

Supplementary Figure S9. XRF core-scanning proxies, core image and lithostratigraphic units defined in the LdM sequence. (a) XRF profiles (Si, S, K, Ca, Ti, Mn, Fe, As, Br, Rb, Sr and Zr expressed as counts per second) (b) The XRF ratios as proxies to identify; layers poor in biogenic carbonate and relatively rich in silicate or BioSi (Si/Ti and Si/Sr), grain-size (Zr/Rb), organic productivity (Br/Ti), sedimentary sulfur/pyrite (S/Ti), redox conditions (Fe/Mn), and carbonate (Ca/Ti) productivity. Three main facies groups: Lacustrine Facies (D1 to D6); Lacustrine Turbidites (LT1 and LT2); Volcanic facies [lapillis (L1 to L5) and tephras (T1 to T18)].

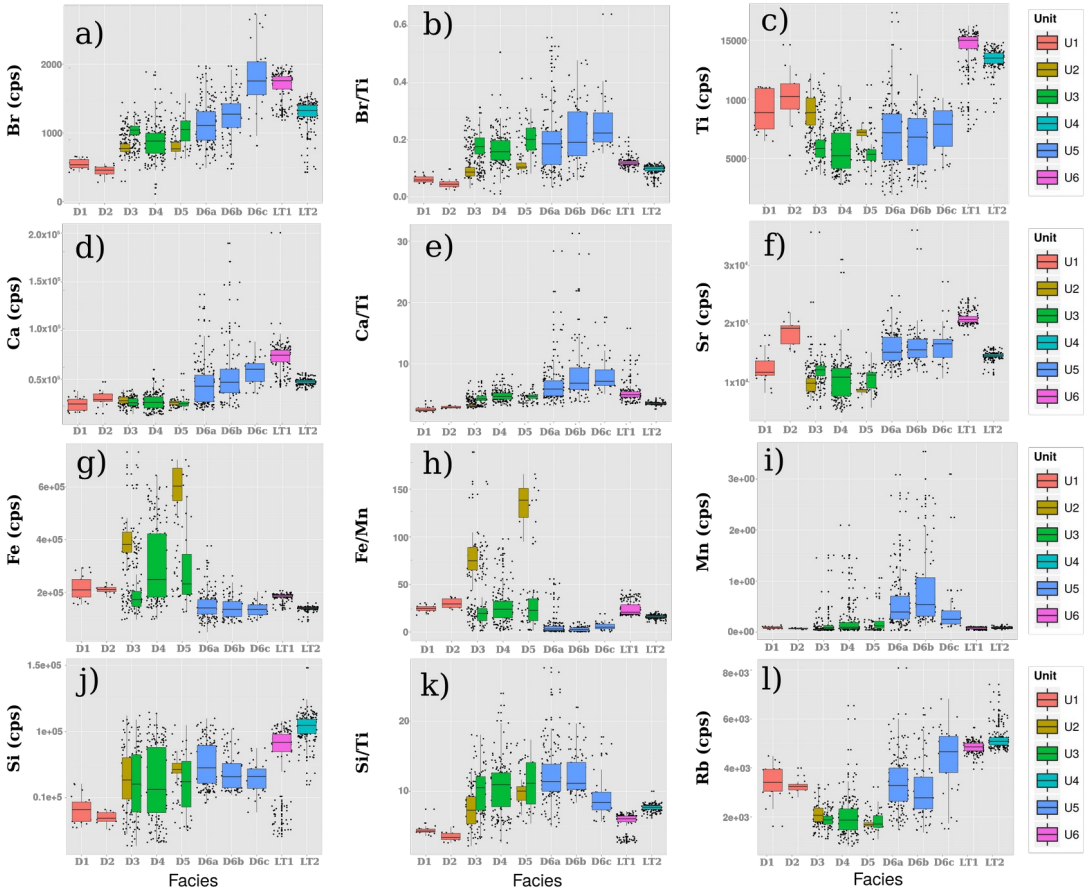

Supplementary Figure S10. Compositional Box-plots of sedimentary facies and units for XRF data. (a)Br (cps); (b) Br/Ti ratio; (c) Ti (cps); (d) Ca (cps); (e) Ca/Ti ratio; (f) Sr (cps); (g) Fe (cps); (h) Fe/Mn ratio; (i) Mn (cps); (j) Si (cps); (k) Si/Ti ratio; (l) Rb (cps). The data were plotted with the R *qqplot* package (Wickham, H., and Chang, W. 2013)

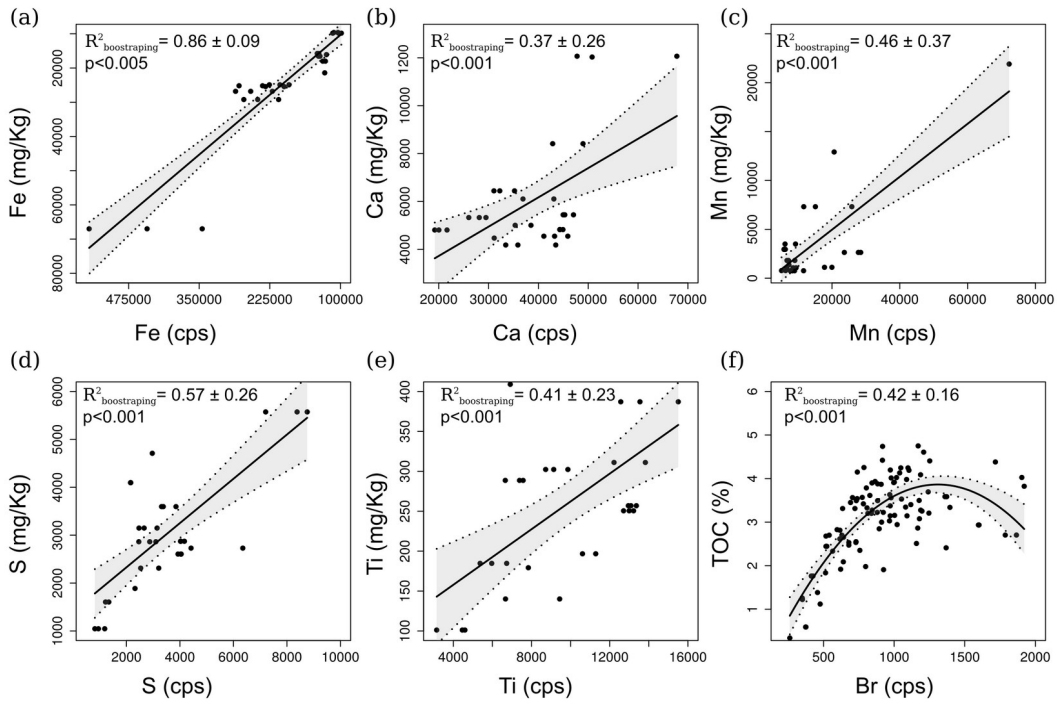

Supplementary Figure S11. Comparison between XRF and ICP data (Ca, Fe, Mn, S and Ti). Regression analyses were performed using an initial split of the data into training and test sets for calculated the $R^2_{boostraping}$ (with 100 iterations). Grey shading indicates 95% confidence intervals. The data were plotted with the R *qqplot* package (Wickham, H., and Chang, W. 2013)

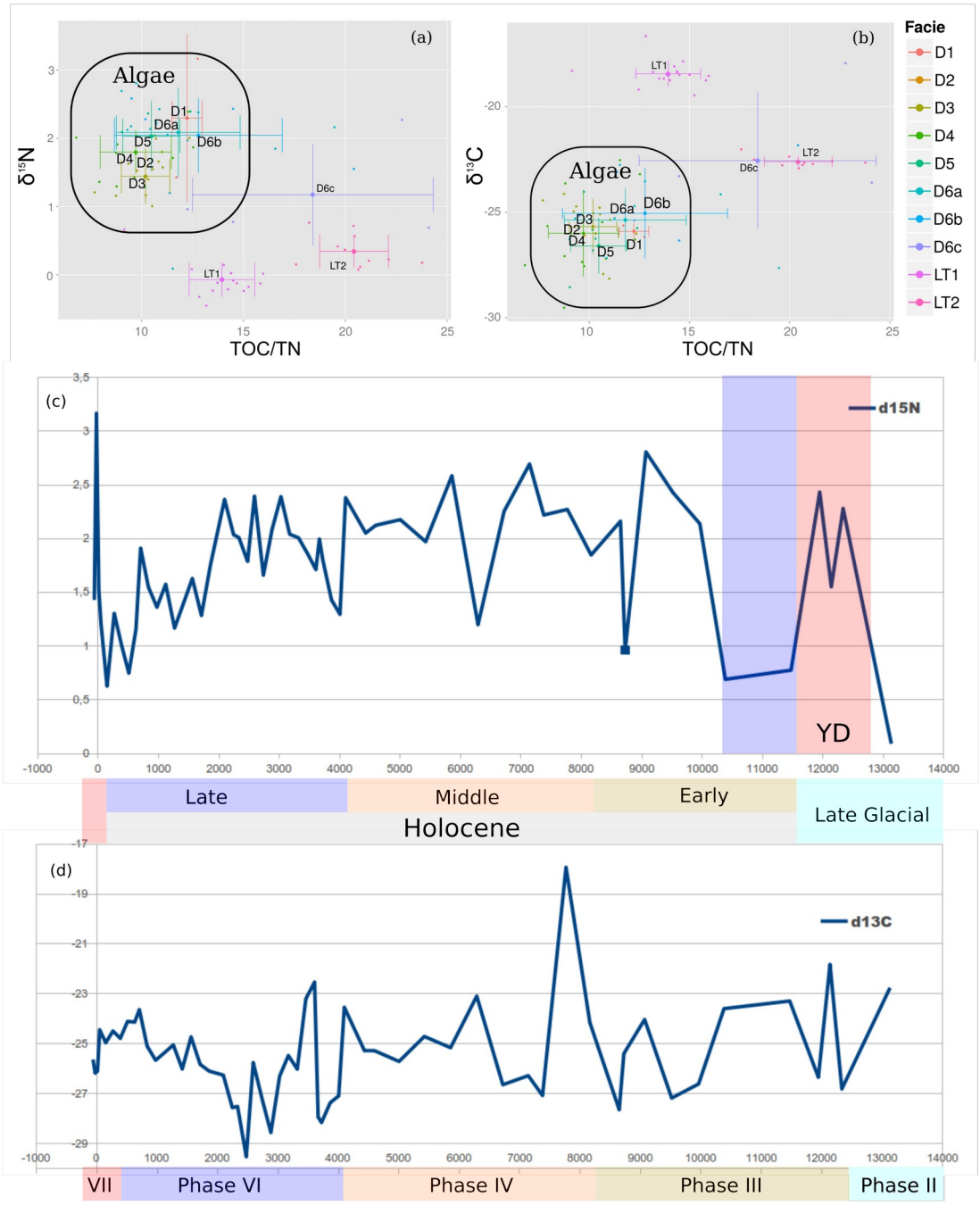

Supplementary Figure S12. Scatter plot of sedimentary facies for $\delta^{13}C$ and $\delta^{15}N$ vs C/N. (a) $\delta^{15}N$ vs C/N ratio and (b) $\delta^{13}C$ vs C/N. Large dots and line indicate the mean and standard deviations, respectively. The data were plotted with the R *qqplot* package (Wickham, H., and Chang, W. 2013). (c) and (d) $\delta^{13}C$ and $\delta^{15}N$ calibrated age (cal BP).

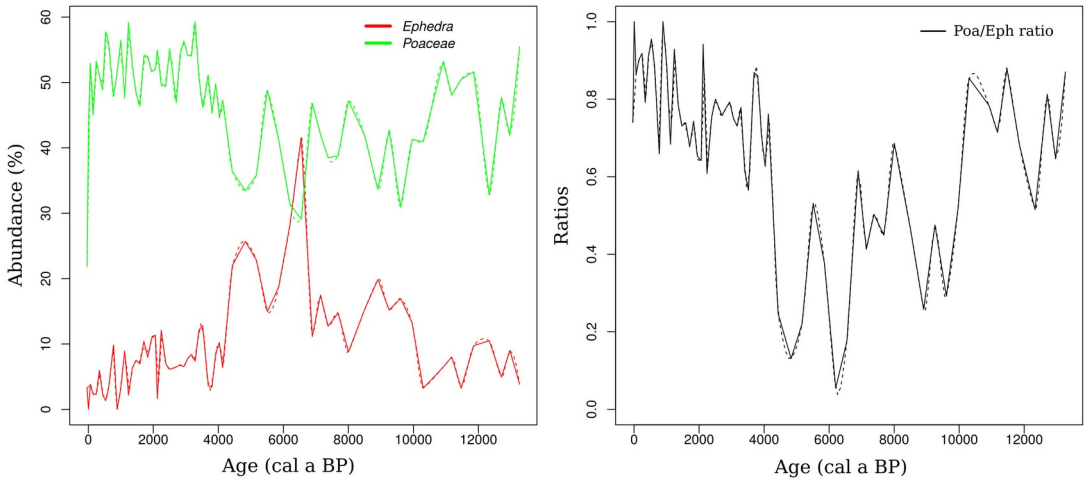

Supplementary Figure S13. Pollen record from LdM sequence. Time series of relative abundances (%) of *Poaceae* and *Ephedra* pollen and *Poaceae/Ephedra ratio* discussed in the text. Ratio use the formula (a−b)/(a+b), where *a* represents *Poaceae* pollen and *b* represent *Ephedra* pollen (Maher,1972; 1963)

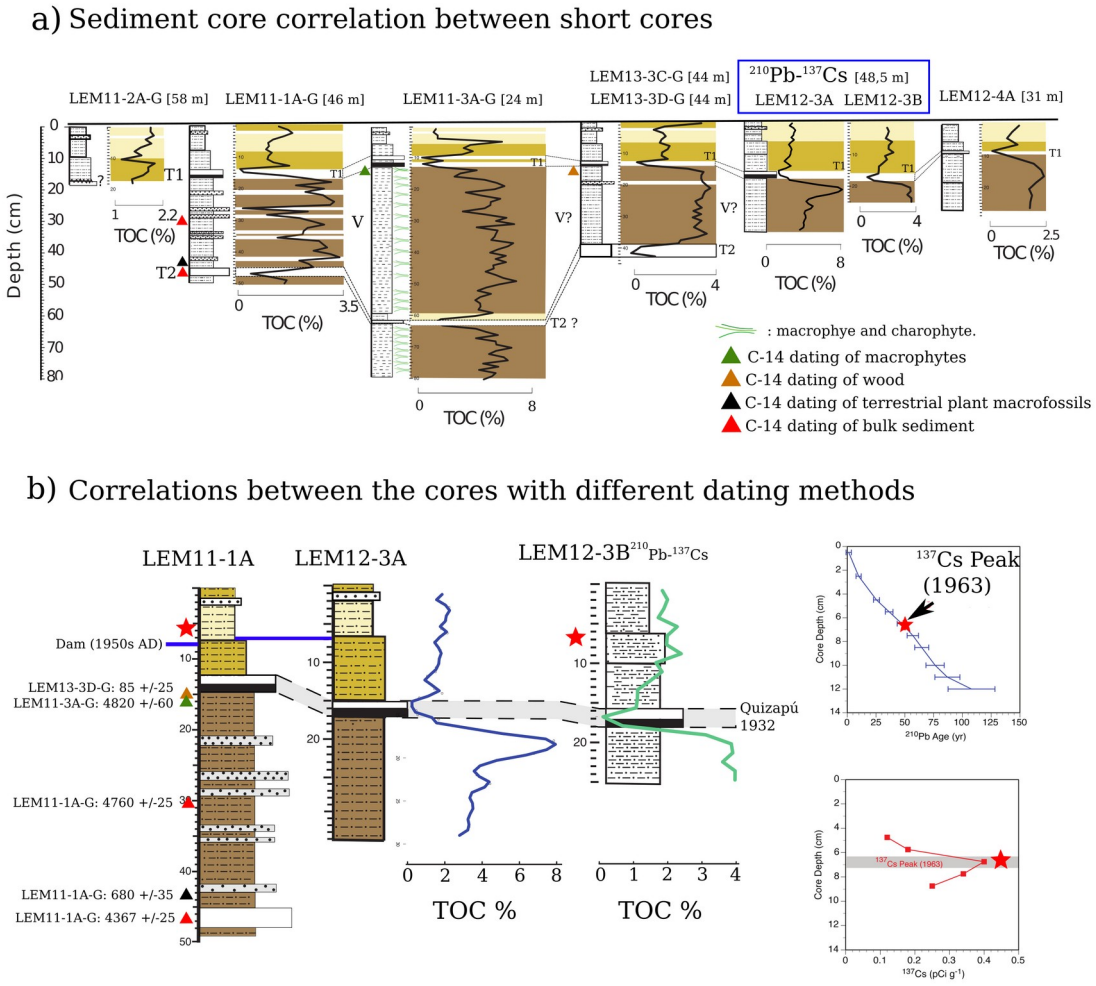

Supplementary Figure S14. a) and b) show the correlations along of a W-E transect of cores in LdM used for determiner the reservoir effect correction. Sedimentary facies, total organic carbon (TOC), radiocarbon dates and correlation using TOC profiles and T1 tephra. Red stars are the peak ^{137}Cs. Triangles green, brown, black and red show the 14C dating of macrophye, wood terrestrial macrofossil and bulk sediment, respectively.

5. Supplementary References

Candès, E. J., Li, X., Ma, Y., Wright, J., 2011. Robust principal component analysis?. Journal of the ACM, **58**(3), 1-37, doi:10.1145/1970392.1970395.

Chawchai, S., Kylander, M.E., Chabangborn, A., Löwemark, L., Wohlfarth, B., 2015. Testing commonly used X-ray fluorescence core scanning-based proxies for organic-rich lake sediments and peat. Boreas, 45(1), 180–189. doi:10.1111/bor.12145

Grimm, E.C., 1987. CONISS: A FORTRAN 77 Program for Stratigraphically Constrained Cluster Analysis by the Method of Incremental Sum of Squares. *Computers & Geosciences*, **13** (1),13–35. doi:10.1016/0098-3004(87)90022-7.

Hubert, M., Rousseeuw, P. J., and Branden, K. V. (2005). Robpca: A new approach to robust principal component analysis. Technometrics, 47(1):64–79.

Kylander, M.E., Ampel, L., Wohlfarth, B., Veres, D., 2011. High-resolution X-ray fluorescence core scanning analysis of Les Echets (France) sedimentary sequence: new insights from chemical proxies. J. Quat. Sci. 26, 109–117. doi:10.1002/jqs.1438

Luebert, F., Pliscoff, P., 2006. Sinopsis bioclimática y vegetacional de Chile. Editorial Universitaria.

Maher, L.J., 1963 Pollen analyses of surface sediments from the southern San Juan Mountains, Colorado. Geol Soc. Am. Bull. 74:1485–1504. doi:10.1130/0016-7606(1963)74[1485:PAOSMF]2.0.CO;2

Pebesma, E. J. 2004. Multivariable Geostatistics in S: The Gstat Package. Computers & Geosciences 30 (7): 683–91. doi:10.1016/j.cageo.2004.03.012

R Core Team (2016). R: A language and environment for statistical computing. R Foundation for StatisticalComputing, Vienna, Austria.URL https://www.R-project.org/.

Simpson, G. L., 2007. Analogue methods in palaeoecology: using the analogue package. J. Stat. Soft., 22(2), 1-29. doi: 10.18637/jss.v022.i02

Wickham, H., Chang, W. 2013. An implementation of the Grammar of Graphics. R package version.